Influence of Microphysical Cloud Parameterizations on Microwave Brightness Temperatures

Gail M. Skofronick-Jackson, *Member, IEEE*, Albin J. Gasiewski, *Senior Member, IEEE*, and James R. Wang, *Senior Member, IEEE*

***Abstract*—The microphysical parameterization of clouds and rain cells plays a central role in atmospheric forward radiative transfer models used in calculating microwave brightness temperatures. The absorption and scattering properties of a hydrometeor-laden atmosphere are governed by particle phase, size distribution, aggregate density, shape, and dielectric constant. This study investigates the sensitivity of brightness temperatures with respect to the microphysical cloud parameterization. Calculated wideband (6–410 GHz) brightness temperatures were studied for four evolutionary stages of an oceanic convective storm using a five-phase hydrometeor model in a planar-stratified scattering-based radiative transfer model. Five other microphysical cloud parameterizations were compared to the baseline calculations to evaluate brightness temperature sensitivity to gross changes in the hydrometeor size distributions and the ice–air–water ratios in the frozen or partly frozen phase. The comparison shows that enlarging the raindrop size or adding water to the partly frozen hydrometeor mix warms brightness temperatures by as much as 55 K at 6 GHz. The cooling signature caused by ice scattering intensifies with increasing ice concentrations and at higher frequencies. An additional comparison to measured Convection and Moisture Experiment (CAMEX-3) brightness temperatures shows that in general all but two parameterizations produce calculated T_Bs that fall within the CAMEX-3 observed minima and maxima. The exceptions are for parameterizations that enhance the scattering characteristics of frozen hydrometeors.**

***Index Terms*—Clouds, electromagnetic scattering, millimeter wave radiometry, rain, remote sensing, snow.**

I. Introduction

OVER the past four decades, significant effort has been devoted to understanding the microphysical cloud characteristics of convective storms (e.g., [1]–[3]). The microphysics of clouds is of considerable interest in a wide range of interdisciplinary studies. These studies include improving global climate models for understanding climate variability, investigating the role of hydrometeors in lightning generation, examining chemical interactions and rain evolution in clouds for pollution research, studying radar and lidar remote sensing applications, and developing precipitation parameter retrievals from satellite-based passive microwave imagery.

Of interest here is improving our understanding of the relationships between the microphysics of hydrometeors in a convective storm and the upwelling microwave brightness temperatures for the purposes of rain rate and precipitation parameter retrieval. A comprehensive understanding of these relationships is hindered by the lack of accurate and sufficiently detailed atmospheric microphysical profile truth [4], [5]. Difficulties in obtaining microphysical cloud profile truth for convective systems stem from limitations in remotely sensed measurements, aircraft sampling capabilities, and the extremely inhomogeneous and complex nature of convection [6], [7]. The dynamics of convection complicate the *in situ* measurements of hydrometeor size, shape, total water content and the ice–air–water ratio, and Nyquist spatial and temporal sampling of these quantities remains a formidable challenge.

A microphysical cloud parameterization used in radiative transfer models requires specifying the size distributions and ice–air–water ratios for each hydrometeor type at each atmospheric level along with vertical profiles of temperature, relative humidity, and pressure. Parameterizations have been developed using statistics from physical models of particle growth and coalescence as well as knowledge from limited *in situ*, radar, and lidar observations. Early cloud parameterizations (e.g., [8]) used in radiative transfer models allowed for a uniform rain layer and separate cloud water layer with no ice particles. Later models added an ice layer (e.g., [9]–[12]).

Contemporary microphysical cloud parameterizations allow for multiple liquid and ice phases (e.g., [2], [4], [13], [14]). Several research studies have indicated that five hydrometeor phases adequately represent a convective storm [5], [15] from the standpoint of passive microwave signatures. The five hydrometeor phases are generally classified as cloud water, rain drops, cloud ice, snow (or ice aggregates), and graupel (including hail). The rain drops are commonly modeled by the Marshall–Palmer (MP) [16] size distribution. However there appear to be no universally accepted size distribution parameterizations or ice–air–water ratios for the other four hydrometeor types [6]. In general, the microphysical parameterizations used by radiative transfer modelers are appropriate for only specific storm occurrences.

As satellite passive microwave sensing of rain rate and other precipitation parameters (e.g., cell top altitude, see [17]) matures, it is important to understand the impact of the various common hydrometeor parameterizations on the upwelling microwave brightness. Accordingly, the purpose of this work is to

Manuscript received January 16, 2001; revised September 18, 2001. This work was supported by NASA Graduate Student Researchers Program (NGT-50903) and NASA Tropical Rainfall Measuring Mission (NAG5-7777), and the National Oceanic and Atmospheric Administration.

G. M. Skofronick-Jackson is with the University of Maryland, Baltimore County, Baltimore, MD 21250 USA and also with NASA Goddard Earth Sciences and Technology Center, Greenbelt, MD 20771 (e-mail: gailsjackson@ieee.org).

A. J. Gasiewski is with NOAA Environmental Technology Laboratory, Boulder, CO 80305 USA.

J. R. Wang is with the Microwave Sensors Branch, NASA Goddard, Greenbelt, MD 20771 USA.

Publisher Item Identifier S 0196-2892(02)01424-9.

study the sensitivity of computed microwave brightness temperatures to changes in the microphysical parameters. The analysis of these changes is facilitated using wideband microwave aircraft data. Since identifying the best parameterization requires detailed collocated and coincident *in situ*, radar, and radiometer observations, we instead focus on identifying a plausible class of parameterizations. Indeed, cloud parameterizations are case specific. The work of [18] and [19] are two examples where parameterizations that best match case-specific radiometer observations have been determined. Even though an optimal parameterization cannot be identified in this study, inappropriate and unrealistic parameterizations can be identified and avoided in future work.

In studying microphysical cloud parameterizations and their effect on computed brightness temperatures, a planar-stratified atmosphere and a midlatitude oceanic surface are assumed. The simple planar model is adequate for all but the most localized cumuluform convection. The highly reflective oceanic background is more uniform and provides greater sensitivity to hydrometeor scattering and absorption than would a land background, and thus represents the more conservative of the two backgrounds. For comparison purposes, four cloud profiles are selected to represent the early cumulus, evolving, mature, and dissipating stages of a convective storm. Six microphysical cloud parameterizations were selected for use in evaluating brightness temperature sensitivities to the hydrometeor size parameters, and frozen particle ice–air–water ratios. A five-hydrometeor-phase (cloud water, rain, cloud ice, dry snow, and dry graupel) parameterization is considered to be the baseline case. Brightness temperatures at twelve frequencies (6.0, 10.69, 18.7, 23.8, 36.5, 89.0, 150.0, 183.31 + 7.0, 220.0, 325 + 8.0, 340.0, and 410.0 GHz) were computed for each of the four cloud stages and six parameterizations using the planar-stratified scattering-based radiative transfer model of [11]. We discuss herein the variations in brightness temperature values when the microphysical cloud parameterization is changed in the radiative transfer calculations.

While convective storms under different prevailing conditions (e.g., tropical, midlatitude, maritime, or continental) have differing hydrometeor characteristics, this study nonetheless identifies several issues. First, in order to select the proper parameterization for any specific condition, one requires a set of detailed atmospheric truth profiles along with a collocated and coincident set of brightness temperature observations. Second, we show the sensitive relationship between the brightness temperature and the underlying hydrometeor profile. In identifying these issues we first briefly describe the radiative transfer model and calculations, including the ocean surface and top-of-atmosphere conditions. Dielectric mixing theory for heterogeneous snow and graupel particles is outlined. Section III details the six microphysical cloud parameterizations. The comparison among the six parameterizations (Section IV) and to the aircraft data (Section V) is described with a summary in Section VI.

II. Radiative Transfer Model

The planar-stratified radiative transfer (RT) model developed by [11] is used to compute the upwelling brightness temperature (T_B) vectors. In this iterative model, scattering is considered to be a perturbation to the clear-air T_B solution [11], [20]. To simplify the analysis the brightness temperature observation angle was assumed to be nadir ($\theta = 0°$), and horizontally finite cloud structures were not considered. Furthermore, the ocean surface wind speed is set to 0.0 m/s and the ocean is assumed to be a specular surface with reflectivity determined using Fresnel coefficients. The aggregate absorption and scattering coefficients of the atmosphere ($\mathcal{K}_a$, $\mathcal{K}_s$, respectively) are obtained from the atmospheric state at each level. The aggregate absorption and scattering coefficients are equal to the algebraic sum of all the individual hydrometeor absorption and scattering coefficients. The algebraic sum can be used because the hydrometeors are randomly distributed and thus scatter incoherently. The aggregate coefficients are given by:

$$\mathcal{K}_a = \kappa_{O_2} + \kappa_{H_2O} + \sum_{h=1}^{H} \kappa_{a_h} \tag{1}$$

$$\mathcal{K}_s = \sum_{h=1}^{H} \kappa_{s_h}. \tag{2}$$

where κ_{a_h} and κ_{s_h} denote the absorption and scattering contributed by an individual atmospheric constituent or hydrometeor type h, and H is the number of hydrometeor types modeled.

The individual absorption (κ_{a_h}) and scattering (κ_{s_h}) coefficients are governed by the size distribution, density, shape, and dielectric constant of both gases and hydrometeors. Water vapor and oxygen absorb electromagnetic radiation as described by [21] and [22], and denoted by $\kappa_{a_{H_2O}}$ and $\kappa_{a_{O_2}}$, respectively. Polydispersive particle size distributions are assumed for the precipitating particles. The absorption and scattering coefficients are determined by integrating the Mie efficiencies over the polydispersive size distribution [23]. In practice, simplified numerical calculations are available using Rayleigh theory [24] for electrically small particles, (i.e., $\langle D \rangle \ll 0.1\lambda/\pi$), where $\langle D \rangle$ is the average diameter and λ is the wavelength. The reformulated Mie equations from [25] are used for electrically large particles.

The particle size distribution (PSD), or number density of particles within the diameter range D to $D + dD$, is modeled by a decaying inverse exponential function

$$N_h(D) = N_{h_0} e^{-\Lambda_h D} \ (\mathrm{cm}^{-4}) \tag{3}$$

where

$$\Lambda_h = [\pi \rho_h N_{h_0} / M_h]^{0.25} \ (\mathrm{cm}^{-1}) = \langle D \rangle^{-1}. \tag{4}$$

In the previous equation, M_h is the content in g/cm^3 of hydrometeor type h, ρ_h is the average intrinsic density in g/cm^3, and N_{h_0} in cm^{-4} is a multiplier. The subscript h is used to distinguish among the various classes of hydrometeors (e.g., ρ_w, ρ_r, ρ_i, ρ_s, and ρ_g for the intrinsic density of cloud water, rain, ice, snow, and graupel, respectively). For large particle diameters (i.e., greater than ~0.5 mm in diameter and for frequencies between ~10 and ~300 GHz the liquid scattering coefficient κ_s is slightly greater than the liquid absorption coefficient κ_a [23];

for smaller particles, liquid absorption is greater than liquid scattering. Ice scattering dominates ice absorption for all microwave frequencies and particle sizes. The relationship between the aggregate scattering coefficient $\mathcal{K}_s$ and aggregate absorption coefficient $\mathcal{K}_a$ can be used to indicate if radiative cooling from scattering or warming from absorption will occur.

The complex dielectric constant needed to compute $\kappa_{s_{j_h}}$ and $\kappa_{a_{j_h}}$ is a function of frequency, temperature, and the constituent materials of the hydrometeor (e.g., water, ice, or a heterogeneous mixture of ice and air and/or water). Dielectric constants for liquid and homogeneous ice hydrometeors are easily obtained using available Debye relaxation formulae or tables [26], [27]. In contrast, heterogeneous hydrometeors require the use of a dielectric mixing theory and one that is appropriate for precipitation-sized particles is the explicit Maxwell–Garnett formula [28] which is equivalent to the implicit Rayleigh mixing formula. Although mixing theories exist for ellipsoidal particles or multilayer spheroidal inclusions [29], the use of such detailed models warrants separate study. The Maxwell–Garnett mixing theory states that given a host material with dielectric constant ϵ_0, and dielectric inclusions ϵ_1, with size $l \ll \lambda$, the effective dielectric constant is:

$$\epsilon_{eff} = \epsilon_0 \left[1.0 + \frac{3.0v\left(\frac{\epsilon_1 - \epsilon_0}{\epsilon_1 + 2\epsilon_0}\right)}{1 - v\left(\frac{\epsilon_1 - \epsilon_0}{\epsilon_1 + 2\epsilon_0}\right)} \right] \tag{5}$$

where v is the volume fraction of the inclusions [29]. In this work we assume temperature-dependent ice–air–water ratios.

The mixing formula (5) breaks down at high frequencies where the wavelength is smaller than the size of the inclusions. A more appropriate dielectric mixing theory for high frequencies is that of [30]; however, such a computationally intensive mixing theory is unnecessary due to constraints on the inclusion size. For large graupel we may have, e.g., $\langle D \rangle = 4$ mm. If we assume that $l \leq \langle D \rangle / 4$, then we can satisfy $l \ll \lambda$ for all but the highest frequencies of concern and the largest particles. Moreover, since the higher frequencies are unable to probe down to the cloud depths where the largest particles exist, the mixing theory in (5) as used in this study is acceptable.

III. Microphysical Cloud Parameterizations

As RT cloud models developed, the complexity of the cloud parameterizations increased from two phases (e.g., [9], [11], [12]) that included only liquid and ice spheres to multiple liquid and ice phases (e.g., [2], [4], [5]) and non spherical ice particles [5]. Within the class of spherical particle models the multiple natural phases of liquid and ice hydrometeors are well represented by a five-phase parameterization that allows for non precipitating cloud water, rain, non precipitating ice, dry snow, and dry graupel. The last of these constituents is essentially hail with entrained air [2], [3]. While the use of spherically symmetric particles is somewhat idealized, this simplification allows the important effects of particle size distribution and dielectric constitution to be considered separately from that of aspherical particle orientation.

TABLE I
Microphysical Size Distribution Parameters

Hydrometeor type	N_{h_0} (cm^{-4})	ρ_h (g/cm^3)	$\langle D \rangle$ (mm)	$\langle r \rangle_{max}$ (mm)
Rain (MP)	0.08	1.0	0.20	4.48
Dry snow	0.04	0.1	0.18	5.94
Dry graupel	0.04	0.4	0.22	5.88

TABLE II
Six Microphysical Cloud Parameterizations

Case	Description
1	Five hydrometeor phase model (baseline) with suspended cloud water, rain, suspended cloud ice (100% ice), dry snow (10% ice, 90% air), and dry graupel (40% ice, 60% air). Particle size distributions are provided in Table 1.
2	Five phase but with rain having a [1] thunderstorm size distribution. This size distribution uses $N_{r0} = 0.014$ cm^{-4} and $\Lambda_r = 14.49 M^{-0.249}$ cm^{-1} in Eq. 3.
3	Five phase but with snow and graupel having a SS [31] size distribution, where $N_{s,g} = 6.4 \times 10^{-3} M^{-1.09}$ cm^{-4} and $\Lambda_{s,g} = 11.9 M^{-0.52}$ cm^{-1}.
4	Five phase but with the ice-air-water ratio of snow being 20-80-0% and the ice-air-water ratio of graupel being 80-20-0%.
5	Five phase but with snow and graupel having liquid percentages as a function of temperature. (See Eq. 6.)
6	Two phase with all liquid summed as MP rain and all frozen hydrometeors summed as SS ice.

For the baseline case, we assume that rain, snow, and graupel hydrometeors have the exponential size distributions of [3] given in (3) and (4) with parameters N_{0_h} and ρ_h given in Table I. The ice–air–water ratios for cloud water, rain, cloud ice, snow, and graupel are 0–0–100%, 0–0–100%, 100–0–0%, 10–90–0%, and 40–60–0%, respectively. The non precipitating particles have a fixed mean diameter of $\langle D \rangle = 0.002$ cm $= (\Lambda)^{-1}$ and the parameters N_{w_0} and N_{i_0} [in (3)] vary to account for the differing contents M_w and M_i.

The six microphysical parameterizations investigated in this study are presented in Table II. All parameterizations use the same underlying storm profile data. The previously described five-phase model with dry snow and dry graupel is considered the baseline case (case 1) because of its general acceptance and use elsewhere [2], [15]. Furthermore, brightness temperature values obtained with this five-phase model are corroborated by low frequency aircraft observations [13]. Parameterizations 2–5 are identical to the five-phase baseline case, except for the modifications described below. Parameterizations 2 and 3 have modified particle size distributions as follows. For parameterization 2, we use the Joss thunderstorm size distribution [1] for rain, and for parameterization 3, we use the Sekhon–Srivastava (SS) size distribution [31] for the dry snow and graupel. The Joss thunderstorm size distribution favors fewer small-sized particles and more large-sized particles than the MP size distribution. For parameterization 3, ice particles are assumed to be

solid spheres with an SS distribution: $N_i = 6.4 \times 10^{-3} M_i^{-1.09}$ (cm^{-4}) and $\Lambda_i = 11.9 M_i^{-0.52}$ (cm^{-1}). The SS size distribution is an equivalent liquid-sphere size distribution for snowflakes near the ground which yields precipitation rates that are consistent with measured snowflake terminal velocities [31]. The SS size distribution leads to more smaller-sized particles than the modified MP distributions of the five-phase case.

There are two parameterizations (4 and 5) with varied air–ice–water ratios in snow and graupel. Parameterization 4 doubles the percentage of snow and graupel such that $\rho_s = 0.2$ g/m^3 and $\rho_g = 0.8$ g/m^3 (i.e., ice–air–water ratios of 20%–80%–0% and 80%–20%–0%, respectively) making the hydrometeors more typical of aggregates and hail [15]. Doubling the ice percentage will increase the scattering coefficient with respect to parameterization 1. Parameterization 5 adds a wetness percentage (W) to the snow and graupel particles as a function of the atmospheric temperature (in K)

$$W(\%) = \begin{cases} 0.0 & \text{for } T \le -15\,^\circ\text{C} \\ T - 258.15 & \text{for } -15\,^\circ\text{C} < T \le 0\,^\circ\text{C} \\ 15.0 & \text{for } T > 0\,^\circ\text{C}. \end{cases} \quad (6)$$

The ice–air–water ratios are adjusted by removing W from the air percentage and adding the same amount to the water percentage. The Maxwell–Garnett dielectric mixing formula is applied twice, once with ice inclusions in an air matrix and then with water inclusions in the air–ice matrix. Adding water will increase the absorption coefficient and cause brightness temperature warming. This "wet" parameterization models snow and graupel absorption within the melting layer. Melting effects are the basis for the bright band in radar meteorology.

Finally, parameterization 6 combines the ice, snow, and graupel into one class of solid spherical frozen hydrometeors with the SS size distribution. Similarly, the rain and cloud water are combined to form a single rain phase with a MP distribution. This parameterization is included to provide intercomparison with the two-phase parameterizations commonly used in many earlier studies.

The microphysical cloud data used in the six cloud parameterizations are from the Goddard Cloud Ensemble (GCE) simulation of a convective tropical squall [2], [32]. The microphysical information at each point in a storm frame includes height, temperature, relative humidity, and the partial density M_h for cloud water, rain, ice, snow, and graupel [32]. The vertical profiles extend from the ocean surface to between 12 and 20 km and have a varying altitude spacing that is smaller (<1 km) where convective clouds exist. At the lower boundary of the GCE profile data a calm ocean surface at 18 °C is assumed. A calm surface is defined by a wind speed ≤7 m/s causing no significant surface roughness. The boundary condition at the top of the atmosphere (at 100 km) is the cosmic background temperature of 2.73 K.

IV. Comparisons

Comparisons focus on four evolutionary profiles from the three-dimensional GCE data. Each of the four evolutionary stages provides a distinct "snapshot" of the storm. The cumulus stage (C) (Fig. 1) has low rain and graupel densities, but significant suspended cloud water. The large cloud water concentration is representative of a storm early in its evolution. The evolving stage (E) (Fig. 1) has much rain but little ice or graupel and represents a storm further in its early development. The mature stage (M) (Fig. 1) has high rain densities at low altitudes (<4 km) and high graupel densities between 4 and 10 km. This profile is representative of a storm at peak convection [2]. Finally, the dissipating stage (D) (Fig. 1) has moderate low-altitude rain and significant graupel at midlevel altitudes. It is representative of a weakening postconvective storm with a developing anvil region. The GCE temperature and relative humidity profiles for the four stages are shown in Fig. 2. The

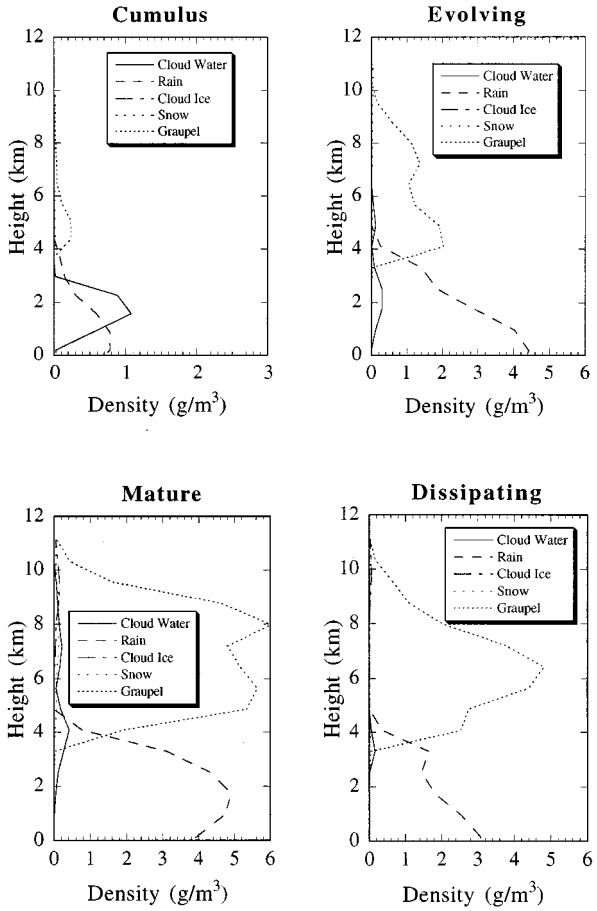

Fig. 1. Microphysical vertical profiles of the cloud water, rain, cloud ice, snow, and graupel densities for stage C, stage E, stage M, and stage D.

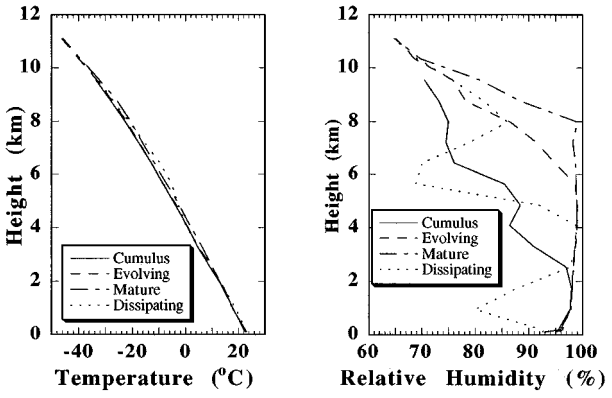

Fig. 2. Temperature and relative humidity profiles for the four cloud stages.

TABLE III
SURFACE RAIN RATES AND INTEGRATED ICE CONTENTS FOR THE FOUR STORM STAGES

Stage	Rain Rate (mm/hr)	Integrated Ice Content (kg/m^2)	Approximate Stage	Symbol
C	10.0742	0.5884	Cumulus	×
E	80.7251	7.6733	Evolving	□
M	111.3941	28.9451	Mature	○
D	50.5127	17.6868	Dissipating	△

temperature profiles show little variation, while the relative humidity profiles show variation similar to the cloud water and rain profiles. The rain rates and integrated ice contents of the four storm stages are provided in Table III.

Nadir brightness temperatures at twelve microwave frequencies (6.0, 10.69, 18.7, 23.8, 36.5, 89, 150.0, 183.310 + 7.0, 220.0, 325 + 8.0, 340.0, and 410.0 GHz) were computed for each of the four stages and six microphysical parameterizations. A comparison of the computed brightness temperature values for each of the frequencies follows in Fig. 3(a)–(l). The plot for each frequency presents the T_B values as a function of the parameterizations. The symbols ×, □, ○, △ indicate storm stage C (cumulus), E (evolving), M (mature), and D (dissipating), respectively. The T_B values are presented as perturbations from clear-air values. Not including the data to the right of the dotted line, (to be discussed in Section V), two tables have been developed to intercompare the parameterizations, storm stages, and T_B values at each frequency. Table IV details the T_B variations for each frequency over the six microphysical parameterizations, while Table V provides a summary of the effects of each parameterization for the four stages. Tables IV and V use parameterization 1 as the reference. A brief textual summary of Fig. 3 and Tables IV and V follows in low to high frequency order.

At 6 GHz, a warming response due to absorption from only the highest densities and thus the largest rain drops is expected. The absorptive signature of rain at 10.69 GHz is significant. Liquid scattering (cooling) occurs when the size of the raindrop exceeds 0.5 mm or the rain rate exceeds ∼30 mm/hr [23]. Thus, the bulk liquid scattering coefficient at 10 GHz is only weakly dependent on the hydrometeor size. Ice scattering should not be a prominent contributor to the signature at 10 GHz unless the density of ice is extremely high [e.g., Fig. 3(b), parameterizations 4 and 6]. At 18 GHz, scattering from only the largest ice particles begins to cause cooling [2], [4]. The 23.8 GHz water vapor channel is very sensitive to cloud water, and the ice scattering signature increases. Thus, the stage with the largest amount of cloud water and the fewest frozen hydrometeors (stage C) shows the warmest T_B values at 23.8 GHz across all parameterizations [Fig. 3(d)]. At 36.5 GHz the effects of ice scattering are considerable and start to cancel the absorptive warming due to rain. For the 89 GHz channel, scattering dominates the spectral signature while liquid water absorption plays only a minor role. Above 89 GHz, the scattering signature is stronger than the absorptive warming signature, and all T_B values are below the clear-air T_B values [negative perturbation values, Fig. 3(g)–(l)]. Above 220 GHz, the T_B variability among all six parameterizations and four stages is reduced. The compression is caused by an increasing sensitivity to hydrometeor size and increasing cloud-top opacity as wavelength decreases. This sensitivity can saturate the response to cloud and hydrometeor particles at these higher frequencies. The large opacity also precludes probing into the highly variable hydrometeors at lower altitudes. The cloud top opacity also explains why the T_B variations of the early cumulus profile (stage C, with its limited ice) are not strongly compressed [Fig. 3(j)–(l)].

Table IV identifies changes of more than 5 K with respect to parameterization 1. This table shows that the Joss PSD (parameterization 2) only affects frequencies at or below 36.5 GHz. The Joss parameterization warms all storm stages at 6 GHz and warms the 10 and 18 GHz channels when the rain rate is low (stages C and D). The Joss PSD cools T_B values at the higher frequencies when the rain rate is high since it produces larger drops that increase scattering.

The SS PSD (parameterization 3) produces warmer T_B values for frequencies at and above 18.7 GHz because the SS PSD generates smaller snow and graupel particles than does parameterization 1. At the lower frequencies only storm stages with significant ice are warmed (stages E, M, D), however at higher frequencies ($\geq$150 GHz), the SS PSD does not change the T_B values of stage M because ice scattering reaches saturation regardless of the ice PSD.

On the other hand, parameterization 4 causes cooling at all frequencies above 6.0 GHz. The increased ice percentage in the snow and graupel particles generates increased scattering. There is less than a 5 K response for storm stage C for frequencies below 36.5 GHz because stage C has little snow and graupel. At 410 GHz saturation results in a minimal variation ($<$5 K) for stage M.

For parameterization 5 the snow and graupel have a variable liquid water fraction, and a general warming of the T_B values occurs. There is a single incidence of a decreased T_B value at 10 GHz. This is likely due to the fact that the "melted" snow and graupel particles appear to be large raindrops at 10 GHz—large enough to cause some scattering. Since the higher frequencies respond to the high-altitude frozen hydrometeors, there is little change in the high frequency T_B values from parameterization 1 to parameterization 5.

Since parameterization 6 combines the snow and graupel contents to form a solid ice spherical particle, the scattering component is greatly increased with respect to the other parameterizations. Thus the storm stages with high ice content have low T_B values (See Table IV). These low T_B values are sometimes 75 K lower than the T_B values for the baseline case [Fig. 3(c), dissipating stage].

Table V reinforces the data in Table IV while providing details of the relationships between storm stage and parameterization. Associated with Table V is a coded summary detailing the T_B changes for each storm type as a function of parameterization.

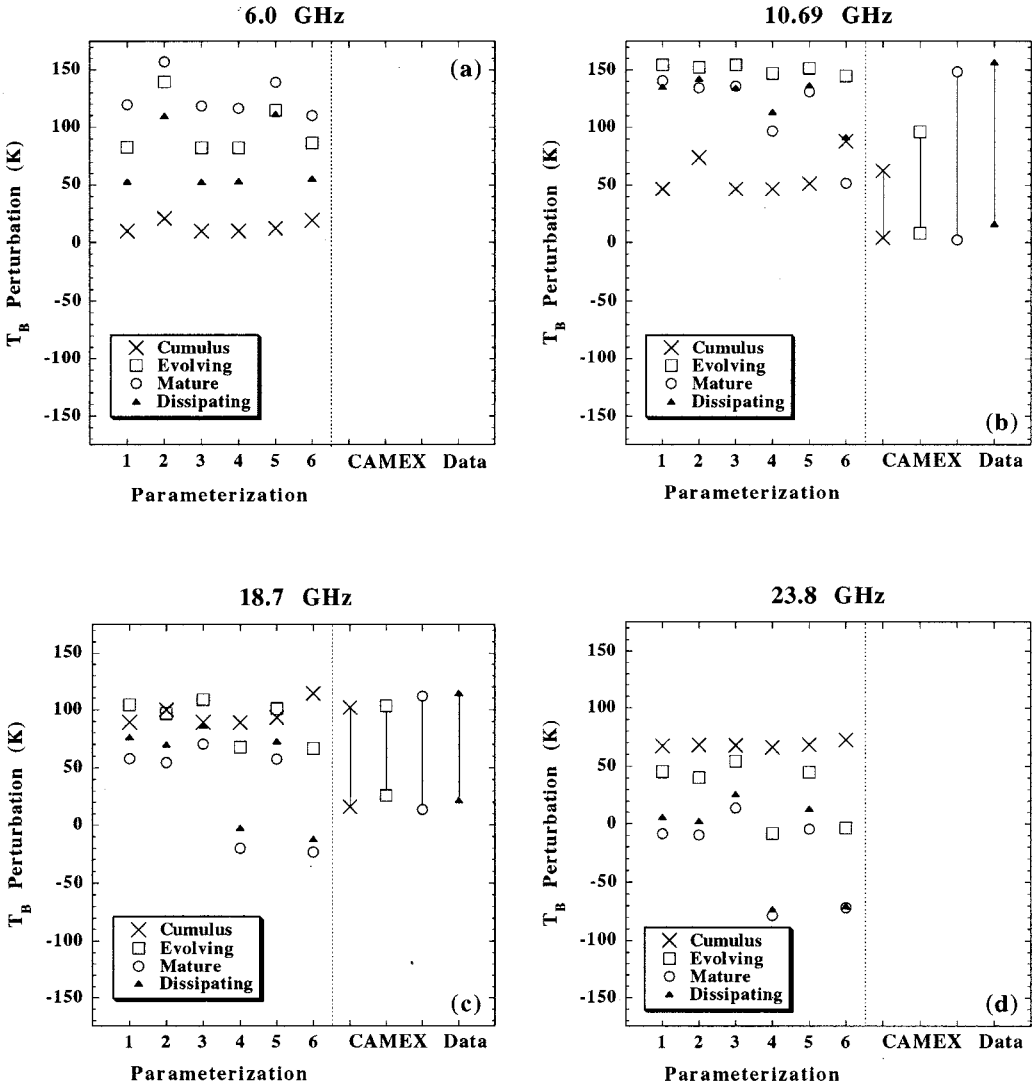

Fig. 3. Brightness temperature perturbations from clear air for the four stages and six parameterizations at (a) 6.0 GHz, (b) 10.69 GHz, (c) 18.7 GHz, and (d) 23.8 GHz. The calculations for the various parameterizations are shown to the left of the dashed line, to the right are the minima and maxima of the observed CAMEX-3 T_B.

V. Aircraft Intercomparisons

In Fig. 3, nadir T_B perturbations from high-altitude aircraft observations are plotted to the right of the dotted line for frequencies where observed data are available. The observations are from the Millimeter-wave Imaging Radiometer (MIR) [33] and the Advanced Microwave Precipitation Radiometer (AMPR) [34] onboard the NASA ER-2. The MIR observed at 89, 150, 183.31 $\pm$ 1, $\pm$3, $\pm$7, 220, and 340 GHz, while the AMPR observed at 10.7, 19.35, 37 and 85.5 GHz. Observations were obtained during the CAMEX-3 experiment [35] on August 26, 1998 and September 17, 1998. The observations are roughly categorized into cumulus, evolving, mature, and dissipating stages. The observed T_B minimum and maximum perturbations (from nearby clear-air observations) are indicated with matching cloud stage symbols and a line joining the minima and maxima. Comparing perturbed values removes the effects of differing ocean surface conditions. Several features of the observed versus computed data are enumerated. First, most of the calculations are within the minimum and maximum observed values indicating that the parameterizations are reasonable in most cases. Second, for 220 and 340 GHz the calculated values are well within the observed minima and maxima for all parameterizations [Fig. 3(i) and (k)]. This observation suggests increasing the complexity of frozen hydrometeor PSD's and their air–ice–water mixtures in simulated cloud profiles and thus expanding the calculated T_B ranges. Next note that for parameterization 4 the calculated T_B values are too cool for most of the stages and frequencies between 18 and 89 GHz [Fig. 3(c)–(f)]. This observation implies that parameterization 4 produces too much ice scattering at the low and middle frequencies. Similarly, the two-phase model (parameterization #6) produces T_B values warmer than the maxima of the 10 and 18 GHz observations for the cumulus and evolving stages and cooler than the minima for most of the stages and the middle frequencies (18–150 GHz). A plausible explanation is that combining the rain and cloud water increases absorptive warming, while combining the cloud ice, snow, and graupel densities increases scattering and cooling. Since parameterization #6 is consistently outside the minima

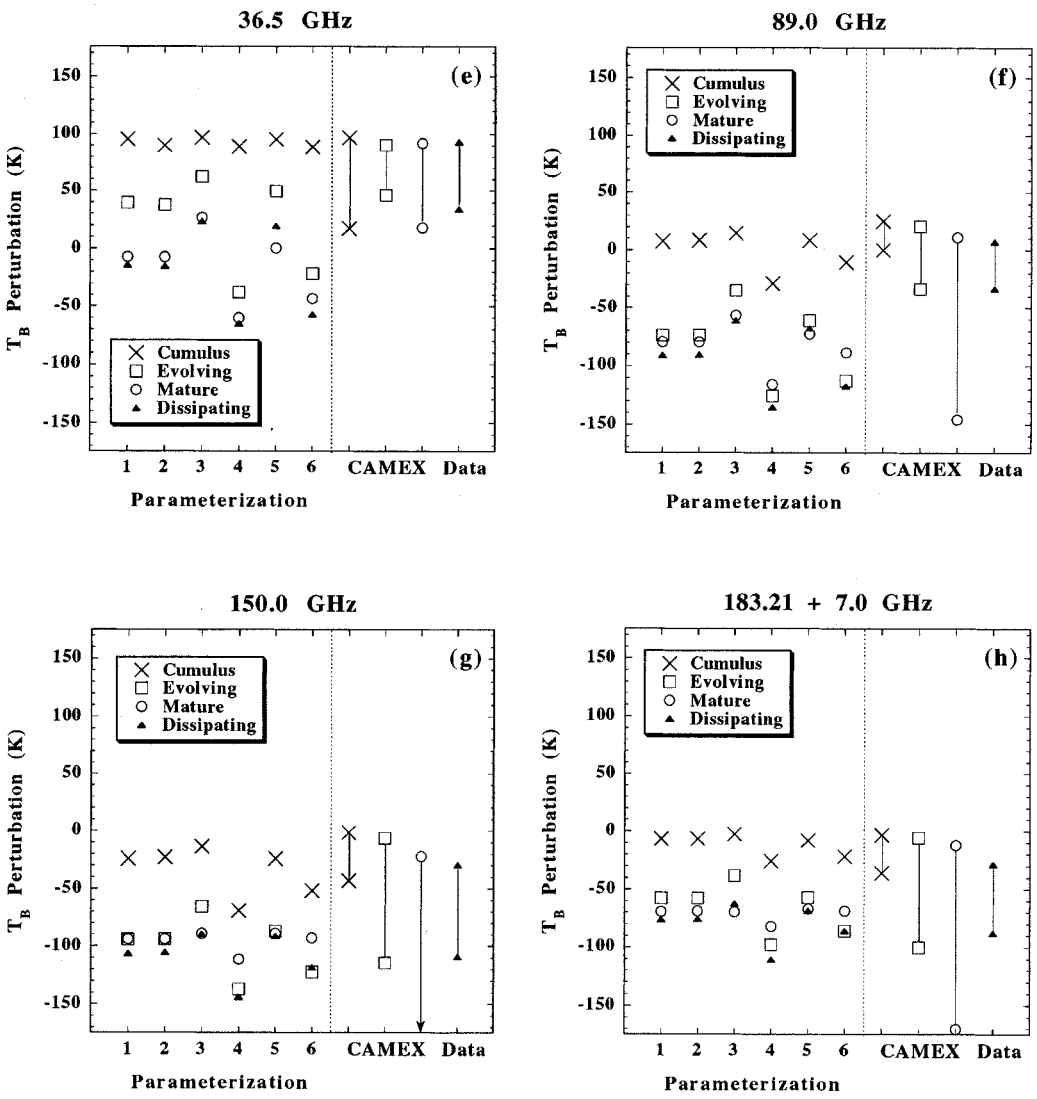

Fig. 3. (*Continued.*) Brightness temperature perturbations from clear air for the four stages and six parameterizations at (e) 36.5 GHz, (f) 89.0 GHz, (g) 150.0 GHz, and (h) 183.31 + 7.0 GHz. The calculations for the various parameterizations are shown to the left of the dashed line, to the right are the minima and maxima of the observed CAMEX-3 T_B.

and maxima of the observations we conclude that it is not as applicable as the others for the cloud conditions observed during CAMEX. Finally, there are several individual stages and frequencies wherein the computed T_B do not fall within the observed minima and maxima, in particular: at 10 GHz for stage E; at 36 GHz for stages M and D; and at 89 GHz for stages E and D. These inconsistencies could mean that the observation stages were inadequately categorized into cumulus, evolving, mature, and dissipating stages or that the parameterizations studied do not model the true microphysics of the observations. Only with detailed coincident T_B observations and *in situ* PSD measurements can some of the inconsistencies be understood.

VI. Summary

Brightness temperatures at twelve frequencies between 6.0 and 410.0 GHz were computed for four storm stages obtained from the simulated GCE model set of [36]. The four profiles used in the comparison represent a convective storm in its early cumulus, evolving, mature, and dissipating stages. The investigation illustrates how specific microphysical cloud parameterizations can affect oceanic microwave brightness temperatures.

The densities of the five hydrometeor types of the GCE data were mapped into six different microphysical cloud parameterizations. The parameterizations were designed to evaluate brightness temperature sensitivity to particle size distributions and ice–air–water ratios. A comparison among the six parameterizations, four convective storm stages, and twelve frequencies was performed. A five hydrometeor-phase parameterization [2], [13] was considered as the baseline case.

The comparisons generally showed that increasing the emphasis of water or rain warmed the brightness temperatures. When the size distribution of rain was changed to that of the Joss *et al.* thunderstorm size distribution (which favors larger particle diameters), the T_B values at 6 GHz were warmed by up to 55 K. At 18 and 23.8 GHz the larger-sized Joss particles initiate liquid scattering more so than the smaller-sized MP size distribution, resulting in a small T_B cooling. From 10.69 GHz to 36.5 GHz, a

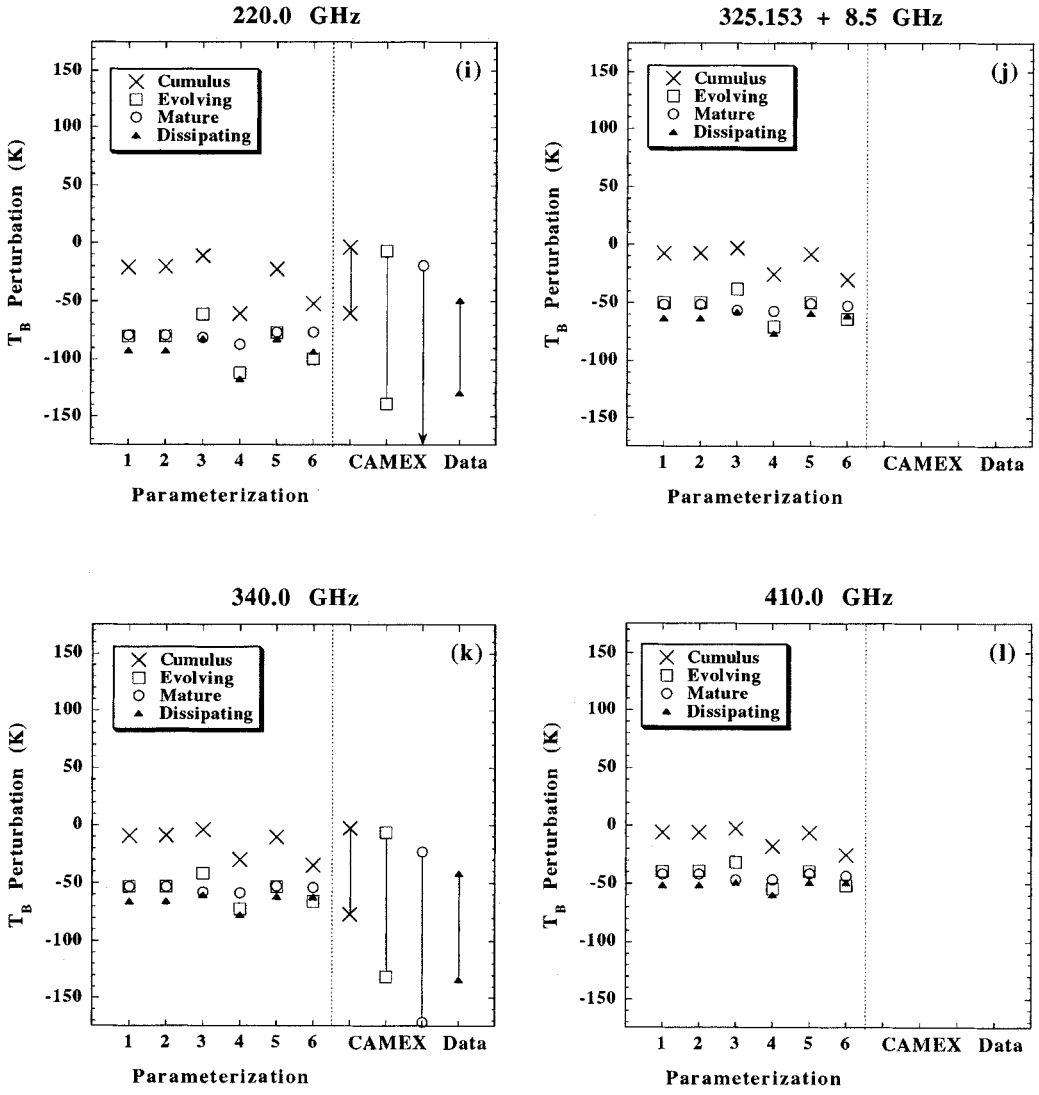

Fig. 3. (*Continued.*) Brightness temperature perturbations from clear air for the four stages and six parameterizations at (i) 220.0 GHz, (j) 325.153 + 8.5 GHZ, (k) 340 GHz, and (l) 410.0 GHz. The calculations for the various parameterizations are shown to the left of the dashed line, to the right are the minima and maxima of the observed CAMEX-3 T_B.

transition from mostly absorptive (characterized by warmer T_B values) to mostly scattering (characterized by cooler T_B values) occurs. At stage C (the early cumulus profile), a change from having the coolest T_B at 10.69 GHz for all parameterizations and pixels (because there is little absorptive warming) to having the warmest T_B values at 36.5 GHz (because there is little scattering) occurs. Above 36.5 GHz changes in the raindrop size distribution initiated no differences in the T_B values with respect to the five-phase model due to the strong scattering signatures of storm-top ice at these higher frequencies. Adding liquid water to the snow and graupel hydrometeors caused absorptive warming at the low and middle frequencies.

From 89 GHz to 220 GHz the scattering signature is stronger than the absorptive warming signature. The comparison showed that the cooling signature due to ice scattering at higher frequencies was increased with larger ice concentrations. The ice concentration rose when additional ice was allocated to the ice–air–water ratio. Above 220 GHz the T_B variability among all six parameterizations and four stages was reduced. The compression was caused by an increasing sensitivity to hydrometeor size as wavelength decreased. This increasing sensitivity caused an increased opacity at the higher frequencies.

Finally, a comparison of the calculated T_B values with available observed T_B values from the CAMEX-3 experiment showed reasonable agreement for most stages and parameterizations. Exceptions occurred for the doubled ice-ratio parameterization and the two-phase parameterization. These two parameterizations consistently yielded T_B values outside the range of the observed minima and maxima, indicating that they are less physically realistic than the others. Another interesting feature is that the 220 and 340 GHz T_B calculations are well within the minima and maxima of the observations, thus providing an argument for increasing the diversity and complexity of frozen hydrometeors in models of convective cloud profiles. (The parameterizations used herein do not provide enough diversity at these frequencies.) Finally, there are a few stages/parameterizations/frequencies whose calculations

TABLE IV
FREQUENCY VERSUS PARAMETERIZATION COMPARISON. STAGES WITH LESS THAN A 5 K DIFFERENCE FROM THE BASELINE FIVE-PHASE PARAMETERIZATION ARE INDICATED BY BLANKS. A "+" ("−") INDICATES A WARMING (COOLING) OF MORE THAN 5 KELVIN WITH RESPECT TO THE BASELINE PARAMETERIZATION

Freq.	Parameterization				
(GHz)	2	3	4	5	6
6.0	+CEMD			+EMD	+C, -M
10.69	+CD, -M		-EMD	-M	+C, -EMD
18.7	+C, -ED	+MD	-EMD		+C, -EMD
23.8		+EMD	-EMD	+D	+C, -EMD
36.5	-C	+EMD	-CEMD	+EMD	-CEMD
89.0		+CEMD	-CEMD	+EMD	-CEMD
150.0		+CED	-CEMD	+ED	-CED
183.31+7.0		+ED	-CEMD	+D	-CED
220.0		+CED	-CEMD	+D	-CE
325.15+8.5		+ED	-CEMD	+D	-CE
340.0		+CED	-CEMD		-CE
410.0		+E	-CED		-CE

TABLE V
(a) SUMMARY OF T_B EFFECTS FOR VARIOUS STORM STAGES AND PARAMETERIZATIONS. COMPARISONS ARE WITH RESPECT TO PARAMETERIZATION 1. (b) CODES FOR (a)

Stage	Parameterization				
	2	3	4	5	6
Cumulus (×)	**a, b**	**e**	**h**	**j**	**p, q**
Evolving (□)	**c, d**	**f**	**i**	**k, l, m**	**q**
Mature (○)	**c, d**	**f, g**	**i**	**k, l, m, n**	**q, r**
Dissipating (△)	**c, d**	**f**	**i**	**l, m, o**	**q, r**

(a)

Code	Effect/Interpretation
a	Joss rain PSD warms $T_B \leq 18.7$ GHz due to increased absorption for the larger drop.
b	The transition from warming due to the larger rain PSD to cooling due to liquid scattering occurs at 36.5 GHz.
c	The upper altitude particles reduce the probing depth at the higher frequencies. Warming due to the larger raindrop size is only seen at 6 GHz.
d	Same as **b**, but at 10.69 to 36.5 GHz depending on upper altitude hydrometeor content.
e	The SS smaller ice sizes warm all window channels $\geq$ 89 GHz.
f	Same as **e** but for frequencies $\geq$ 18.7 GHz due to additional ice in the profile.
g	For the mature stage and frequencies $\geq$ 150 GHz ice scattering saturation occurs for the size distributions of both parameterizations 1 and 3.
h	Since stage C has little ice, doubling the ice ratio only affects $\geq$ 36.5 GHz.
i	Doubling the ice ratio increases scattering and reduces T_B for frequencies $\geq$ 10.69 GHz.
j	Stage C has a minimally thin melting layer, therefore no significant T_B changes.
k	Cloud top ice hydrometeors cause saturation and produce nearly the same T_B for stages E, M and frequencies > 150 GHz.
l	Warming due to increased liquid water content for 36.5—150 GHz.
m	Warming response is reduced above 89 GHz because the high altitude large ice particles preclude probing into the melting layer.
n	Cooling at 10.7 GHz because snow/graupel appear as large raindrops (see **b**).
o	Same as **k** except for 6.0 GHz and 23.8—325 GHz.
p	Absorptive warming due to larger particles of the combined cloud water and rain.
q	The combined ice, snow, and graupel generate larger particles and increase scattering.
r	Scattering saturation causes no significant T_B change at higher frequencies.

(b)

do not fall within the observed minima and maxima. These few inconsistent cases could mean that the clouds were inadequately categorized into cumulus, evolving, mature, and/or dissipating stages or that the parameterizations are not modeling the true cloud microphysics for all cases. A detailed coincident set of T_B observations and *in situ* PSD measurements might be used to further refine cloud microphysical parameterizations.

Some implications of this study on radiative transfer modeling should be noted. First, this study shows that a variety of parameterizations are appropriate for brightness temperature calculations. However, extreme parameterizations (e.g., when ice is over emphasized) produce calculated T_B values outside the range of those observed over midlatitude storms. Second, the observed T_B values show larger ranges of variation than do the calculated T_B values, suggesting that more variety in particle types and sizes might be needed for accurate modeling. Finally, the brightness temperature sensitivity to particle parameters drops at wavelengths shorter than ∼1 mm (e.g., at ∼325 GHz and higher frequencies). This final point supports the potential for using submillimeter wavelength channels to retrieve cirrus ice particles.

ACKNOWLEDGMENT

The authors would like to thank Dr. J. Simpson, Dr. W.-K. Tao, and N. Prasad of the NASA/Goddard Space Flight Center, Greenbelt, MD, for providing the Goddard Cumulus Ensemble (GCE) three-dimensional microphysical cloud data. The authors would also like to thank the Global Hydrology Resource Center and R. Hood of the NASA Marshall Space Flight Center for providing the AMPR data. Finally, they would like to thank W. Manning of the University of Maryland, Baltimore County, Baltimore, for organizing the combined CAMEX datasets.

REFERENCES

[1] J. Joss, J. C. Thams, and A. Waldvogel, "The variation of raindrop size distributions at Locarno," in *Proc. Int. Conf. Cloud Physics*, Toronto, ON, Canada, 1968, pp. 369–373.

[2] R. F. Adler, H.-Y. M. Yeh, N. Prasad, W.-K. Tao, and J. Simpson, "Microwave simulations of a tropical rainfall system with a three dimensional cloud model," *J. Appl. Meteorol.*, vol. 30, pp. 924–953, July 1991.

[3] S. A. Rutledge and P. V. Hobbs, "The mesoscale and microscale structure and organization of clouds and precipitation in midlatitude cyclones. XII: A diagnostic modeling study of precipitation development in narrow cold-frontal rainbands," *J. Atmos. Sci.*, vol. 41, pp. 2949–2972, 1984.

[4] E. A. Smith, A. Mugnai, H. J. Cooper, G. J. Tripoli, and X. Xiang, "Foundations for statistical-physical precipitation retrieval from passive microwave satellite measurements. Part I: Brightness temperature properties of a time-dependent cloud-radiation model," *J. Appl. Meteorol.*, vol. 31, pp. 506–531, 1992.

[5] K. F. Evans, J. Turk, T. Wong, and G. L. Stephens, "A bayesian approach to microwave precipitation profile retrieval," *J. Appl. Meteorol.*, vol. 34, pp. 260–279, Jan. 1995.

[6] Y.-H. Kuo, J. F. Bresch, M.-D. Cheng, J. Kain, D. B. Parsons, W.-K. Tao, and D. L. Zhang, "Meeting summary: Summary of a mini workshop on cumulus parameterization for mesoscale models," *Bull. Amer. Meteorol. Soc.*, vol. 78, no. 3, pp. 475–491, Mar. 1997.

[7] H. Landsburg, "Variability of the precipitation processes in time and space," in *ASTM Special Tech. Publ. Conf.: Sampling and Analysis of Rain* Philadelphia, PA, Oct. 1981, pp. 3–9.

[8] T. T. Wilheit, A. T. C. Chang, M. S. V. Rao, E. B. Rodgers, and J. S. Theon, "A satellite technique for quantitatively mapping rainfall rates over the oceans," *J. Appl. Meteorol.*, vol. 16, pp. 551–560, 1977.

[9] T. T. Wilheit, A. T. C. Chang, J. L. King, E. B. Rodgers, R. A. Nieman, B. M. Krupp, A. S. Milman, J. S. Stratigos, and H. Siddalingaiahi, "Microwave radiometric observations near 19.35, 92 and 183 GHz of precipitation in Tropical Storm Cora," *J. Appl. Meteorol.*, vol. 21, pp. 1137–1145, 1982.
[10] J. A. Weinman and R. Davies, "Thermal microwave radiances from horizontally finite clouds of hydrometeors," *J. Geophys. Res.*, vol. 83, no. C6, pp. 3099–3107, 1978.
[11] A. J. Gasiewski and D. H. Staelin, "Numerical modeling of passive microwave O_2 observations over precipitation," *Radio Sci.*, vol. 25, pp. 217–235, 1990.
[12] P. Bauer and P. Schluessel, "Rainfall, total water, ice water, and water vapor over sea from polarized microwave simulations and special sensor microwave/imager data," *J. Geophys. Res.*, vol. 98, pp. 20737–20 759, 1993.
[13] G. M. Skofronick-Jackson and A. J. Gasiewski, "Nonlinear statistical retrievals of ice content and rain rate from passive microwave observations of a simulated convective storm," *IEEE Trans. Geosci. Remote Sensing*, vol. 33, pp. 957–970, July 1995.
[14] B. S. Ferrier, W.-K. Tao, and J. Simpson, "A double-moment multiple-phase four-class bulk ice scheme. Part ii: Simulations of convective storms in different large-scale environments and comparisons with other bulk parameterizations," *J. Atmos. Sci.*, vol. 52, pp. 1001–1033, Apr. 1995.
[15] M. McCumber, W.-K. Tao, J. Simpson, R. Penc, and S.-T. Soong, "Comparison of ice-phase microphysical parameterization schemes using numerical simulations of tropical convection," *J. Appl. Meteorol.*, vol. 30, pp. 985–1004, 1991.
[16] J. S. Marshall and W. McK. Palmer, "The distribution of raindrops with size," *J. Meteorol.*, vol. 5, pp. 165–166, 1948.
[17] A. J. Gasiewski and D. H. Staelin, "Statistical precipitation cell parameter estimation using passive 118-ghz O_2 observations," *J. Geophys. Res.*, vol. 94, no. D15, pp. 18 367–18 378, 1989.
[18] N. Prasad, H.-Y. M. Yeh, R. F. Adler, and W.-K. Tao, "Microwave and infrared simulations of an intense convective system and comparison with aircraft observations," *J. Appl. Meteorol.*, vol. 34, pp. 153–174, 1995.
[19] R. Meneghini, H. Kumagai, J. R. Wang, T. Iguchi, and T. Kozu, "Microphysical retrievals over stratiform rain using measurements from an airborne dual-wavelength radar-radiometer," *IEEE Trans. Geosci. Remote Sensing*, vol. 35, pp. 487–506, May 1997.
[20] K.-N. Liou, *An Introduction to Atmospheric Radiation*. San Diego, CA: Academic, 1980.
[21] H. J. Liebe, "A contribution to modeling atmospheric millimeter-wave properties," *Frequenz*, vol. 41, pp. 31–36, 1987.
[22] P. W. Rosenkranz, "Interference coefficients for overlapping oxygen lines in air," *J. Quant. Spectrosc. Radiat. Transf.*, vol. 39, pp. 287–297, 1988.
[23] A. J. Gasiewski, "Microwave radiative transfer in hydrometeors," in *Atmospheric Remote Sensing by Microwave Radiometry*, M. A. Janssen, Ed. New York: Wiley, 1993, pp. 91–144.
[24] W. J. Wiscombe, "Improved Mie scattering algorithms," *Appl. Opt.*, vol. 19, pp. 1505–1509, 1980.
[25] D. Diermendjian, *Electromagnetic Scattering on Spherical Polydispersions*. New York: Elsevier, 1969.
[26] J. A. Lane and J. A. Saxton, "Dielectric dispersion in pure polar liquids at very high radio frequencies," *Proc. R. Soc. London A*, vol. 213, pp. 400–408, 1952.
[27] S. G. Warren, "Optical constants of ice from the ultraviolet to the microwave," *Appl. Opt.*, vol. 23, pp. 1206–1225, 1984.
[28] C. F. Bohren and L. J. Battan, "Radar backscattering by inhomogeneous precipitation particles," *J. Atmos. Sci.*, vol. 37, pp. 1821–1827, 1980.
[29] A. H. Sihvola, "Self-consistency aspects of dielectric mixing theories," *IEEE Trans. Geosci. Remote Sensing*, vol. 27, pp. 403–415, July 1989.
[30] G. H. Goedecke and S. G. O'Brien, "Scattering by irregular inhomogeneous particles via the digitized Green's function algorithm," *Appl. Opt.*, vol. 27, no. 12, June 1988.
[31] R. S. Sekhon and R. C. Srivastava, "Snow size spectra and radar reflectivity," *J. Atmos. Sci.*, vol. 27, pp. 299–307, 1970.
[32] W.-K. Tao and J. Simpson, "Goddard cumulus ensemble model. Part I: Model description," *Terrestrial, Atmos. Oceanic Sci.*, vol. 4, pp. 35–72, 1993.
[33] P. Racette, R. F. Adler, J. R. Wang, A. J. Gasiewski, D. M. Jackson, and D. S. Zacharias, "An airborne millimeter-wave imaging radiometer for cloud, precipitation and atmospheric water vapor studies," *J. Atmos. Oceanic Technol.*, vol. 13, pp. 610–619, 1996.
[34] R. W. Spencer, R. E. Hood, F. J. LaFontaine, E. A. Smith, R. Platt, J. Galliano, V. L. Griffin, and E. Lobl, "High-resolution imaging of rain systems with the advanced microwave precipitation radiometer," *J. Atmos. Oceanic Technol.*, vol. 11, pp. 849–857, 1994.
[35] B. Geerts, G. M. Heymsfield, L. Tian, J. B. Halverson, A. Guillory, and M. I. Mejia, "Hurricane Georges's landfall in the Dominican Republic: Detailed airborne Doppler radar imagery," *Bull. Amer. Meteorol. Soc.*, vol. 81, pp. 999–1018, May 2000.
[36] W. K. Tao and J. Simpson, "Modeling study of a tropical squall-type convective line," *J. Atmos. Sci.*, vol. 46, pp. 177–202, 1989.

Gail M. Skofronick-Jackson received the B.S. degree in electrical engineering from Florida State University, Tallahassee in 1986, and the M.S.E.E. and Ph.D. degrees from Georgia Institute of Technology, Atlanta, GA, in 1988 and 1997, respectively.

From 1988 to 1990, she was an Associate Research Engineer with BellSouth Services, Atlanta. She returned to the Georgia Institute of Technology in 1990 as a Graduate Research Assistant. She joined the Universities Space Research Association as part of the Goddard Visiting Scientist Program, NASA Goddard Space Flight Center, Greenbelt, MD, in 1997. She is currently with the University of Maryland, Baltimore County, Goddard Earth Science and Technology Center, Baltimore, MD. Her research interests include passive remote sensing, radiative transfer theory, and microphysical cloud profile modeling and retrievals.

Dr. Skofronick-Jackson is a member of the American Meteorological Society and the American Geophysical Union.

Albin J. Gasiewski (M'88–SM'95) received the B.S. and M.S. degrees in electrical engineering and the B.S. degree in mathematics, all from Case Western Reserve University, Cleveland, OH, in 1983, and the Ph.D. degree in electrical engineering and computer science from the Massachusetts Institute of Technology, Cambridge, in 1989.

From 1989 to 1997, he was a Faculty Member within the School of Electrical and Computer Engineering, Georgia Institute of Technology (Georgia Tech), Atlanta. He was an Associate Professor at Georgia Tech, where he taught courses on electromagnetics, remote sensing, instrumentation, and wave propagation theory. He is currently with the NOAA Environmental Technology Laboratory, Boulder, CO, where he is Acting Chief of the ETL Microwave Systems Development Division. His technical interests include passive and active remote sensing, radiative transfer theory, electromagnetics, antennas and microwave circuits, electronic instrumentation, meteorology, and oceanography.

Dr. Gasiewski is a member of the IEEE Geoscience and Remote Sensing Society's AdCom, was General Chair of the second Combined Optical-Microwave Earth and Atmosphere Sensing Symposium (1995), and Technical Program Committee Chair of the 20th International Geoscience and Remote Sensing Symposium (IGARSS 2000). He is a member of Eta Kappa Nu, Tau Beta Pi, URSI (Commission F), Sigma Xi, the American Meteorological Society, COSPAR, and the American Geophysical Union. He served on the U.S. National Research Council's Committee on Radio Frequencies (CORF) from 1989 to 1995 and is the author or co-author of 52 publications in the area of electromagnetic remote sensing.

James R. Wang (M'86–SM'91) received the B.S degree in physics from the University of Washington, Seattle, in 1963, and the M.S. and Ph.D. degrees in physics from the University of Chicago, Chicago, IL, in 1964 and 1969.

He has been with the Microwave Sensors Branch, NASA Goddard Space Flight Center, Greenbelt, MD, since 1977. His research interest is primarily in the applications of both active and passive microwave techniques for remote sensing of geophysical parameters such as soil moisture, water vapor, clouds, and precipitation.